RSC Advances

PAPER

View Article Online
View Journal | View Issue

Cite this: *RSC Adv.*, 2018, **8**, 36161

Enhanced photocatalytic performance of spherical BiOI/MnO_2 composite and mechanism investigation

Qingjie Zhou, Lizhu Zhang,* Pengjian Zuo, Yang Wang and Zhenjiang Yu

In this paper, a novel flower-like BiOI/MnO_2 composite was synthesized by two simple steps. The crystal structure, morphology, surface element analysis, and optical properties of as-prepared samples were determined by X-ray diffraction (XRD), scanning electron microscopy (SEM), transmission electron microscopy (TEM), X-ray photoelectron spectroscopy (XPS) and UV-Vis diffuse reflectance spectrometry (DRS). Photocatalytic activities of the prepared photocatalysts were evaluated by photocatalytic degradation of RhB under simulated light irradiation. When 50 mg of a BiOI/MnO_2 composite with a mass ratio of 5/1 was used to degrade RhB aqueous solution (100 mL, 20 mg L^{-1}), the degradation efficiency could reach 99.18% within 60 min under simulated solar light irradiation. In addition, the photocatalyst exhibited good stability. After four cycles, the degradation efficiency of the BiOI/MnO_2 (5/1) composite could reach 92.8% within 80 min. The probable photocatalytic mechanism of photocatalysts was investigated by active species trapping experiments and photoluminescence (PL) measurements. The results showed that the superior photocatalytic activity of the BiOI/MnO_2 composite is derived from the generation and transfer of photogenerated carriers between MnO_2 and BiOI.

Received 19th August 2018
Accepted 9th October 2018

DOI: 10.1039/c8ra06930a

rsc.li/rsc-advances

1. Introduction

In recent years, with increasing discharge of wastewater, the composition of pollutants in wastewater is becoming more and more complex. A large number of toxic and harmful organic pollutants are discharged into the water environment which are difficult to be thoroughly degraded. These pollutants include synthetic dyes, drugs, personal care products and some toxic intermediate products of chemical engineering which caused serious harm to the ecological environment. At the same time, the government and public have more stringent requirements for water quality; the national sewage discharge standards are gradually improving, and the upgrading work continues to grow. Therefore, it is urgent to develop efficient and economical wastewater treatment technology. Advanced oxidation technology has attracted the attention of environmental circles at home and abroad due to its strong oxidation capacity and high efficiency. Among them, a photocatalyst based on semiconductors has the desirable characteristics of mild reaction conditions, simple operation and wide applications. It is considered to be a promising wastewater treatment technology for the treatment of refractory organic pollutants.

Among semiconductor catalysts, BiOI has attracted a large number of investigations as an intriguing semiconductor photocatalyst due to the narrow band gap (1.85–1.96 eV) and strong response to visible light.[1–4] In addition, nanostructured BiOI has better photocatalytic activity than bulk BiOI because of its higher quantum efficiency and specific surface area.[5] At present, there are many ways to synthesize BiOI. For example, J. M. *et al.* synthesized different morphologies of bismuth oxide (BiOI) by microwave irradiation and conventional coprecipitation.[6] Jia Lu *et al.* prepared a tetragonal BiOI photocatalyst by controlling the amount of water in the hydrolysis process.[7] Prakasit Intaphong *et al.* synthesized BiOI nanosheets by a sonochemical method.[8] Although the photocatalytic activity of BiOI is relatively good, the photogenerated electrons and holes easily recombine due to the small band gap, which hinders its application.[9] Therefore, the modification of BiOI is a promising research topic in the field. It is generally known that semiconductor combination, which allows the construction of a heterojunction between two different semiconductors with matching energy band gaps, is an efficient way to separate photoinduced carriers and improve the photocatalytic efficiency of a catalyst. Recently, many heterojunctions for BiOI, such as BiOI/TiO_2,[10] BiOI/BiOBr,[11] and BiOI/Ag@Ag,[12] have been reported and have demonstrated their enhanced photocatalytic activity. Therefore, constructing a heterojunction is a promising way to improve the photocatalytic activity of BiOI.

In many oxide semiconductors, MnO_2 has attracted significant attention as a photocatalyst, lithium battery and supercapacitor due to its low toxicity, low cost, environmental compatibility, abundant availability, narrow band gap, excellent electrochemical performance and higher theoretical

School of Chemistry and Chemical Engineering, Harbin Institute of Technology, Harbin 150001, China. E-mail: zlz4513@sina.com

capacitance.[13–17] In recent years, the application of MnO_2 as a photocatalyst has become more and more popular.[17] For example, Yu *et al.* prepared an MnO_2/ZnO composite by firing at 600 °C.[15] Liu *et al.* prepared a flower-like BiOI/MnO_2 composite by regulating pH. However, the degradation efficiency of 0.1 g of the catalyst prepared by Liu *et al.* is only 94.4% in 40 minutes for RhB solution (100 mL, 10 mg L^{-1}).[18] In general, these preparation methods lack practical significance due to the toxic, complex procedures, expensive reagents or long time requirements. In addition, agglomeration occurs easily during the synthesis process for low dimensional nanomaterials, leading to decrease in surface area and photocatalytic active sites.[19,20]

Given this situation, three-dimensional layered heterojunction materials are considered due to their good catalytic performance and large surface volume. In this paper, we develop a facile method to fabricate a BiOI/MnO_2 composite with a 3D heterojunction by depositing BiOI nanoparticles onto the lamellae of flower-like MnO_2. The obtained BiOI/MnO_2 composite shows observably enhanced photocatalytic performance for the degradation of RhB in aqueous solution under simulated solar light irradiation. When 50 mg of the BiOI/MnO_2 (5/1) composite is used to degrade RhB aqueous solution (100 mL, 20 mg L^{-1}), the degradation efficiency can reach 99.18% within 60 min under simulated solar light irradiation. Furthermore, the probable mechanism of degradation in the presence of BiOI/MnO_2 composites and the process of charge separation and transfer at the surface or interface are also discussed in detail. In addition, the successful synthesis of the BiOI/MnO_2 composite provides an important reference for the synthesis of BiOX (Cl, Br) with MnO_2.

2. Experimental

2.1 Preparation of catalyst

2.1.1 Synthesis of pure MnO_2. MnO_2 samples were prepared following a previously reported procedure.[21] Typically, the $KMnO_4$ (316 mg) and $MnSO_4 \cdot H_2O$ (113 mg) were added into 60 mL of deionized water. Then, the above solution was transferred to a Teflon-lined autoclave (70 mL capacity) and maintained at 120 °C for 12 h. Finally, the black precipitate was dried at 60 °C for 12 h after adequate washing with ethanol and distilled water.

2.1.2 Preparation of different mass ratios of BiOI/MnO_2 composites and pure BiOI. BiOI/MnO_2 composites with different mass ratios (5/2, 5/1, 6/1) were synthesized by a simple procedure.[22] In brief, 0.1 g of as-prepared MnO_2 nano-flowers was ultrasonically suspended in 30 mL of deionized water. Meanwhile, certain amounts of $Bi(NO_3)_3 \cdot 5H_2O$ (0.3446, 0.6892, 0.8271 g) were dissolved in 30 mL of glycol under ultrasound, separately, and this solution was poured into the MnO_2 suspension. Finally, corresponding amounts of KI (0.1179, 0.2357, 0.2830 g) were added dropwise to the above solution, and the mixture was stirred for 5 h, centrifuged and dried. A series of BiOI/MnO_2 samples with different mass ratios were obtained.

The procedure for the synthesis of pure BiOI was the same as above.

2.2 Characterization and photocatalytic performance

2.2.1 Characterization of materials. In this paper, the crystallinity of the prepared materials was analysed by X-ray diffraction analysis (XRD; Holland Panalytical Analytical Instrument Co., Ltd.). Scanning electron microscopy (SEM) was used to analyse the morphology and size of the prepared materials. The lattice parameters and bursts of materials were analysed by transmission electron microscopy (TEM). UV-Vis light (UV-Vis) diffuse reflectance spectra were recorded on a UV-Vis spectrometer. It was necessary to roughly estimate the width of the material by the corresponding transformation. Photoluminescence spectroscopy (PL) was used to analyse the recombination of photo-generated electrons and holes.

2.2.2 Photocatalytic activity. The photocatalytic activity of the prepared materials was monitored toward the degradation of an aqueous solution of rhodamine B (RhB) under visible light generated from a Xe lamp (λ > 420 nm, 300 W, PLS-SXE300, Beijing Berfield Technology Co., Ltd.). In a typical case, 50 mg of the samples was put in RhB (100 mL, 20 mg L^{-1}) solution. Prior to the photocatalytic reaction, the suspensions were adequately stirred in the dark for 30 min to achieve equilibrium of absorption–desorption between the prepared photocatalyst and RhB. Afterward, the Xe lamp was turned on, and 4 mL of the liquid was taken with a 4 mL syringe at a certain time. Then, the catalyst and the solution were separated with a 0.22 micron nylon 66 filter membrane. Finally, UV-Vis spectrophotometry was performed to determine the concentration of RhB by measuring the absorbance at 550 nm. The degradation efficiency of the catalyst was calculated by the following formula:

$$\text{Degradation efficiency (\%)} = (C_0 - C)/C_0 \times 100\%$$

C_0 is the initial concentration of the RhB aqueous solution, and C is the concentration of the aqueous solution at time t.

The stability of the catalyst was determined by the following experiments: the photocatalyst of BiOI/MnO_2 (5/1) after photocatalysis was centrifuged for collection, washed with water and ethanol three times to remove residual impurities, and then dried at 60 °C for recycling.

3. Results and discussion

3.1 Structure and morphology characterization

The XRD patterns of MnO_2, BiOI and BiOI/MnO_2 composites are presented in Fig. 1. The characteristic diffraction peaks of BiOI at 29.6°, 31.7°, 45.4° and 55.2° are assigned to the (102), (110), (200) and (212) crystal planes, respectively, as indexed by (JCPDS 10-0445).[1] XRD analysis confirms the monoclinic lamellar structure of birnessite-type MnO_2 (JCPDS 42-1317) with mixed crystalline and amorphous parts. Two broad peaks at 2θ of around 12.6° and 36.2° can be indexed to birnessite-type MnO_2.[23] Broad peaks indicate a poorly crystallized compound. Meanwhile, the intensities of the MnO_2 peaks decrease with the increase in the mass ratio of the BiOI/MnO_2 composite, which might be ascribed to the relatively low amount and weak diffraction intensity of MnO_2 in the BiOI/MnO_2 composites.[24]

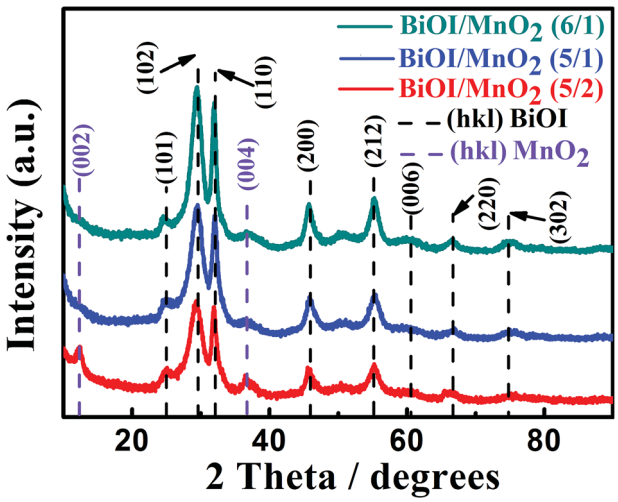

Fig. 1 XRD patterns of the as-prepared BiOI, MnO_2 and different mass ratios of BiOI/MnO_2 composites.

The morphology and structure of MnO_2, BiOI and BiOI/MnO_2 composites were observed by scanning electron microscopy (SEM) and transmission electron microscopy (TEM). The SEM images of MnO_2, BiOI and BiOI/MnO_2 composites are shown in Fig. 2. It can be observed that the morphology of pure MnO_2 was similar to that of pure BiOI. Both are typical flower-like structures at the micron scale stacked from nanosheets with uniform morphology. Fig. 2(b)–(e) show the SEM results of BiOI/MnO_2 composites. The morphology of the BiOI/MnO_2 nanocomposite exhibits a structure in which BiOI nanospheres are supported on sheets of flower-like MnO_2 with intimate contact. With the increase in the mass ratio of the BiOI/MnO_2 composite, the lamellas of MnO_2 are almost covered by spherical BiOI. This may lead to a situation where iodine yttrium oxide occupies the active site of manganese dioxide, which in turn affects the photocatalytic effect of the composite. Transmission electron microscopy (TEM) was used to analyze the morphology of the heterojunction. From the TEM images (Fig. 2(h) and (i)), one can see the transparent nanosheets, indicating that the ultra-thin MnO_2 nanosheets are synthesized, and some spheres can be directly observed. The HRTEM image demonstrates three sets of lattice fringes with inter-planar spacings of 0.351 nm, 0.301 nm and 0.915 nm, which correspond to the (002) plane of MnO_2 and (102) and (001) planes of BiOI. Thus, it can be concluded that the BiOI/MnO_2 composites are successfully fabricated. The result of the EDS analysis (Fig. 3) is in accordance with the elements of BiOI/MnO_2 (5/1). Table 1 shows the composition of 4 elements of the BiOI/MnO_2 (5/1) composite. It can be observed that the mass ratio of the BiOI/MnO_2 composite is about 5/1.

The XPS spectra of the BiOI/MnO_2 (5/1) composite were obtained to identify the elemental composition and valence state of surface elements. In Fig. 4, the Mn 2p spectrum displays two distinct peaks with corresponding binding energy values of 642.1 eV and 653.7 eV. These binding energy values are assigned to the spin orbit double of Mn $2p_{3/2}$ and Mn $2p_{1/2}$, which is

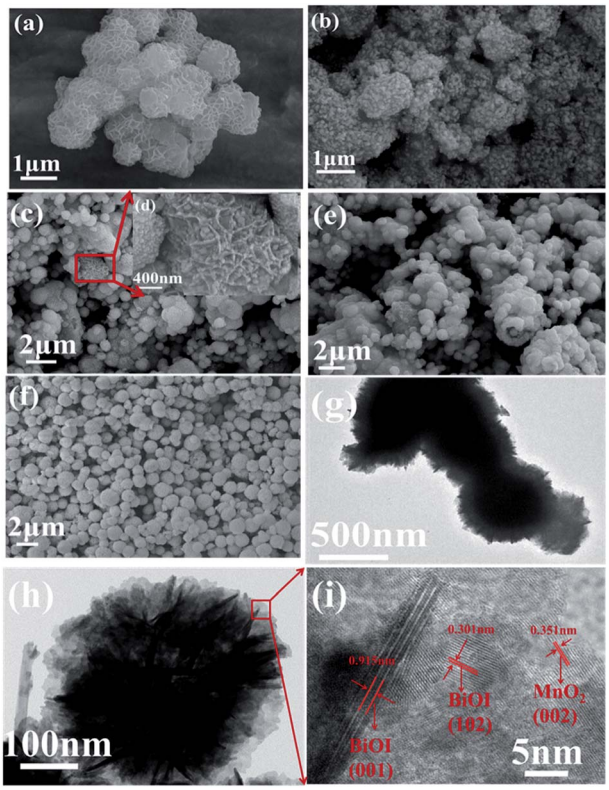

Fig. 2 SEM images of photocatalysts: (a) pure MnO_2, (b) BiOI/MnO_2 (5/2), (c) BiOI/MnO_2 (5/1); (d) high magnification images of the BiOI/MnO_2 (5/1) composite, (e) BiOI/MnO_2 (6/1), (f) pure BiOI; (g) TEM image of BiOI/MnO_2 (5/1) and (h) amplified TEM image of BiOI/MnO_2 (5/1); (h) magnified TEM image and (i) HRTEM image of BiOI/MnO_2 (5/1) composite.

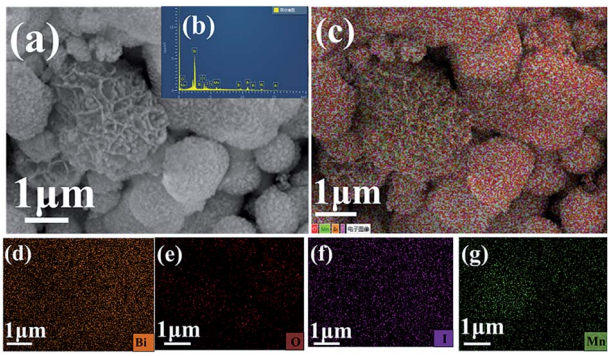

Fig. 3 (a) SEM image of BiOI/MnO_2 (5/1) heterojunction; (b) EDS elemental spectrum of the as-prepared BiOI/MnO_2 (5/1) heterojunction; (c) EDS mapping of all elements in the BiOI/MnO_2 (5/1) heterojunction; (d)–(g) maps of the distribution of each element: (d) bismuth, (e) oxygen, (f) iodine, (g) manganese.

Table 1 Table of the composition of BiOI/MnO_2 (5/1) composite

Element	wt%	Atomic percent(%)
O	10.13	48.88
Mn	9.24	12.97
I	35.07	21.32
Bi	45.57	16.83
Gross	100	100

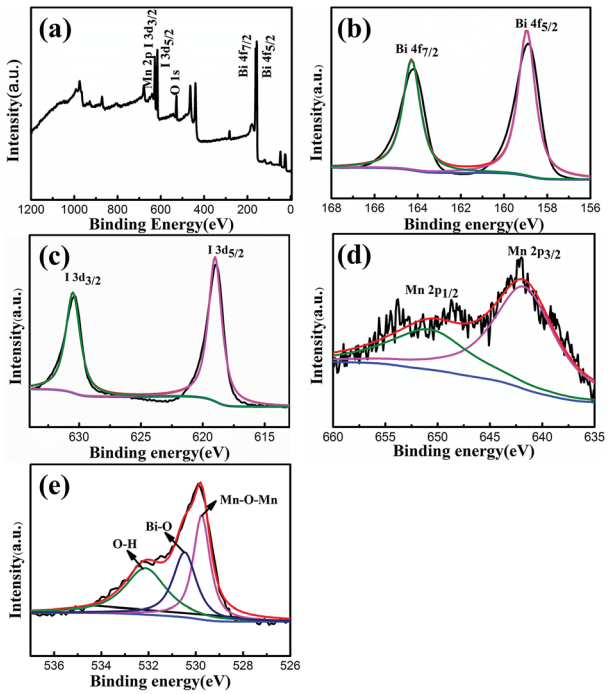

Fig. 4 (a) Survey XPS spectrum and high-resolution XPS spectra of BiOI/MnO_2 (5/1), (b) Bi 4f, (c) I 3d, (d) Mn 2p, (e) O.

consistent with the results of MnO_2.[25] In the O 1s spectrum (Fig. 4(e)), three different peaks centered at 529.9 eV, 530.4 eV, and 531.8 eV are assigned to Mn–O–Mn bonds in MnO_2,[25] Bi–O bonds[26] in $[Bi_2O_2]^{2+}$ slabs of the BiOI structure, and Mn–O–H,[25] respectively. In the XPS spectra of Bi 4f, the two strong peaks at 158.8 eV and 164.1 eV correspond to Bi $4f_{5/2}$ and Bi $4f_{7/2}$, which is consistent with the valence state of Bi^{3+} in BiOI.[1] As demonstrated in Fig. 4(c), the two peaks in the I region of 619 eV and 630.5 eV are consistent with I $3d_{5/2}$ and I $3d_{3/2}$,[1] respectively, which correspond to the characteristics of I in BiOI.

3.2 Optical absorption properties

The photocatalytic performance is relevant to the energy band structure of a semiconductor.[27] The optical properties of BiOI, MnO_2 and BiOI/MnO_2 composites are depicted in Fig. 5. Pure BiOI displays strong photo-absorption from UV light to visible light shorter than 660 nm, and its band-gap energy, revealed in the inset, is approximately 1.8 eV. Bare MnO_2 can absorb from ultraviolet to visible light, and its band-gap energy is about

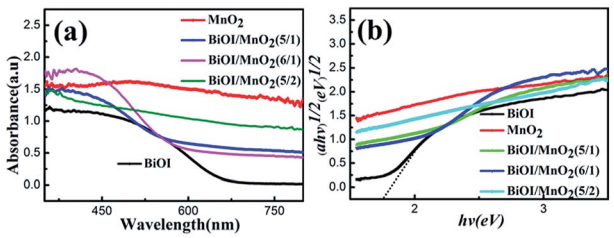

Fig. 5 (a) UV-Vis diffuse reflectance spectra of pure BiOI, MnO_2 and different mass ratios of BiOI/MnO_2 samples; (b) graphical evaluation of band gaps of as-prepared photocatalysts.

0.25 eV.[18] With the combination of BiOI and MnO_2, the absorbance edges of BiOI/MnO_2 present a red shift compared to that of pure BiOI. Fig. 5(b) shows that the band gap of the composites is narrower than that of pure BiOI. The results from DRS indicate that the photocatalysts possess good photocatalysis activity.

3.3 Catalytic activity of BiOI/MnO_2

To evaluate the performance of photocatalysis of the as-prepared samples, the adsorption capacity of the catalysts was determined by mixing with RhB aqueous solution in darkness within 30 minutes. From Fig. 6(a), we could conclude that the suspensions reached adsorption–desorption equilibrium within 30 minutes. The pure BiOI sample absorbed about 71.4% of RhB in 30 min. When the mass ratio of BiOI to MnO_2 was 5/1, the highest adsorption performance of RhB was achieved. This phenomenon may be related to their special BET and surface areas (47.6 $m^2\ g^{-1}$). Then, degradation of RhB was carried out under simulated sunlight irradiation (300 W Xe lamp, $\lambda > 420$ nm). Clearly, self-degradation of RhB can be ignored according to Fig. 7(b). The degradation rate of RhB was only 12.6% over MnO_2, which was due to the narrow band gap of MnO_2 resulting in the high recombination of photo-generated electrons and holes. On the other hand, the BiOI/MnO_2 composites showed excellent degradation activity. Two hours later, under simulated sunlight, the degradation efficiencies of RhB were 92.3%, 100%, and 100% for the 5/2, 5/1, and 6/1 BiOI/MnO_2 composites, respectively. Especially for the BiOI/MnO_2 composite (5/1), the removal rate was 99.18% in 60 minutes; it required only 80 min to degrade completely. The catalytic performance of the physically mixed BiOI and MnO_2 (marked as BiOI + MnO_2 (5 + 1)) was also observed. After two hours, the degradation efficiency of the mixture to RhB aqueous solution was 73%. This confirmed the

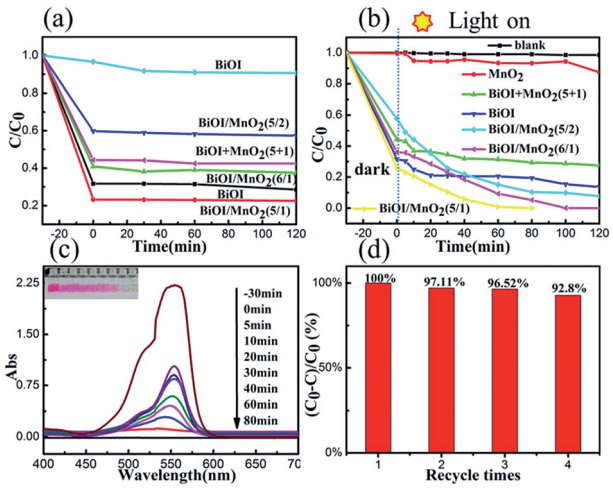

Fig. 6 (a) Adsorption of RhB under dark conditions, (b) degradation curves of RhB under visible light irradiation, (c) temporal UV-Vis absorption spectra of RhB after being illuminated by simulated solar light from −30 min to 80 min in the presence of BiOI/MnO_2 (5/1), (d) recycling photocatalytic test of BiOI/MnO_2 (5/1) photocatalysts for photodegradation of RhB four times under simulated solar light irradiation. Reaction conditions: 50 mg samples, 100 mL of 20 mg L^{-1} RhB aqueous solution, reaction time 80 min.

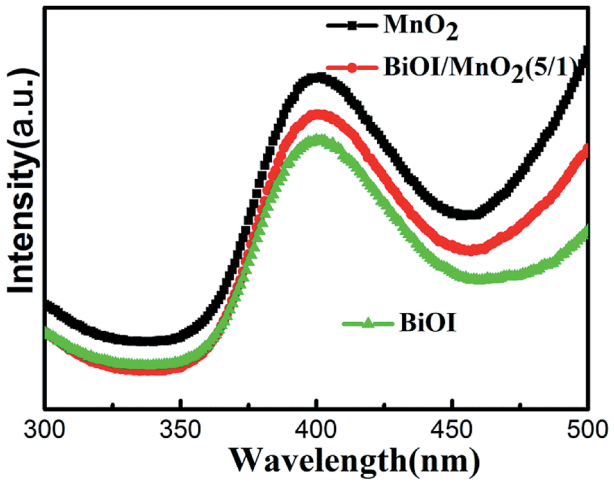

Fig. 7 PL emission spectra of pure BiOI, BiOI/MnO_2 (5/1) composite, and MnO_2.

interaction between BiOI and MnO_2 to improve photocatalytic performance. Detailed photocatalytic mechanisms are further discussed in the photocatalytic mechanism section.

Furthermore, we also measured the long-term cyclic performance of the BiOI/MnO_2 (5/1) composite to detect the stability of the material. After each cycle, the amount of catalyst was weighed. It was found that the amount of the reduction of the catalyst after each cycle was less than 1%. The result of degradation is shown in Fig. 6(d), demonstrating slight decrease (<10%) in degradation of RhB under visible-light irradiation after four cycles; this indicated high stability of the material. As is shown in Fig. 6(c), the main peak of RhB (λ = 550 nm) completely disappeared only after 80 min of irradiation. Moreover, the color of the supernatant changed from red to colorless, observed by the naked eye, verifying the excellent photocatalytic activity of MnO_2/BiOI (5/1) under visible light irradiation. Such a result is much better than that of bare BiOI and MnO_2.

3.4 Possible photocatalytic mechanism

The photocatalytic reaction involves a series of processes, in which the carrier recombination probability greatly affects the photocatalytic activity. Photoluminescence (PL) is a common method to study carrier separation, migration and recombination and has an important application to reveal the reaction mechanism of photogenerated electron–hole pairs in semiconductor photocatalysts.[28] When the semiconductor is excited by light, the electrons in the valence band are transferred to the conduction band. The electrons in the conduction band have high energy. The electrons return to the valence band during the annealing process. When the photo-electrons return to the valence band and combine with the holes, the photons are radiated, thus producing photoluminescence. Therefore, the high intensity of a PL emission spectrum corresponds to a relatively high carrier recombination probability. The low intensity of a PL emission spectrum corresponds to a relatively low carrier recombination probability. Fig. 7 shows the PL emission spectra of BiOI, MnO_2, and the BiOI/MnO_2 (5/1) composite. The excitation source wavelength is 260 nm. As shown in Fig. 7, the PL spectra indicate that the samples integrated with BiOI can decrease the intensity of the peaks of MnO_2 due to the formation of a BiOI/MnO_2 (5/1) heterojunction. The carriers can effectively transfer at the interface of BiOI and MnO_2, thus restraining the recombination rate of the photogenerated carriers. In addition, the spectrum shows that BiOI has lower carrier recombination efficiency than BiOI/MnO_2 (5/1). But the degradation efficiency of BiOI is lower than that of BiOI/MnO_2 (5/1) composite. Combining the UV-Vis spectrum, the possible reason is that BiOI absorbs less visible light, resulting in fewer photogenerated electrons and holes.

To reveal the roles played by active species in the photodegradation of RhB by the BiOI/MnO_2 composite, we use ascorbic acid (VC),[29] iso-propanol (IPA),[30] and ammonium oxalate (AO) as $\cdot O^{2-}$, $\cdot OH$, and h^+ scavengers, respectively. The addition of IPA hardly inhibits RhB degradation. However, the presence of ascorbic acid and ammonium oxalate reduces the degradation efficiency of the catalysts in varying degrees (Fig. 8).

Three active species trapping experiments indicate that both h^+ and $\cdot O^{2-}$ play important roles in the degradation of RhB, and their contribution to RhB degradation is $h^+ > \cdot O^{2-}$. In addition, this shows that $\cdot OH$ hardly contributes to the process of degradation.

Based on the above experimental results, the possible photocatalytic mechanism of the BiOI/MnO_2 composite was proposed. The band gap of BiOI is calculated to be 1.8 eV. According to the literature, the band gap of manganese dioxide is 0.25 eV.[18] The conduction band and valence band edge values of BiOI were calculated to be about 0.47 eV and 2.37 eV, whereas the corresponding values of MnO_2 were 1.33 and 1.58 eV. Accordingly, the possible photocatalytic mechanism for the high-efficiency BiOI/MnO_2 composite is proposed in Fig. 9. Interestingly, the band structures of BiOI and MnO_2 showed matching band positions, forming a heterojunction. The formation of a heterojunction was considered as an effective means of carrier separation, which could improve photocatalytic performance.[31] As displayed in Fig. 9, the conduction band (0.47 eV) of BiOI was more negative than the conduction band (1.33 eV) of MnO_2, which was thermodynamically beneficial for the transfer of photo-generated charge carriers.

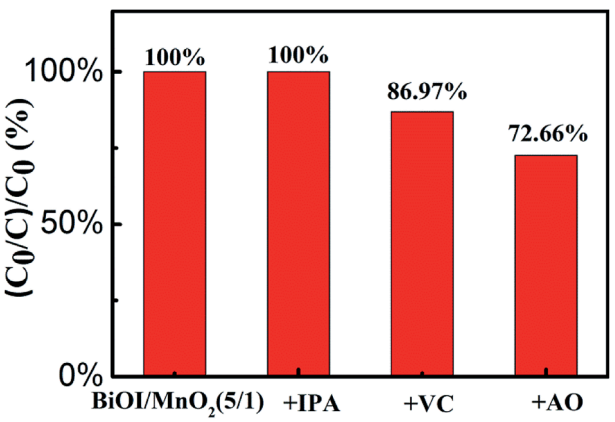

Fig. 8 Effects of different scavengers on the degradation of RhB over BiOI/MnO_2 (5/1) composite.

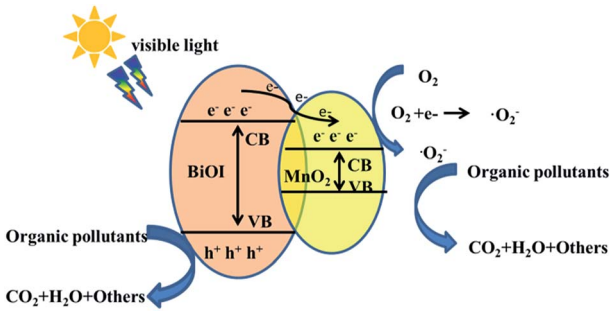

Fig. 9 The proposed possible mechanism for the improvement of photocatalytic activity.

Under visible light irradiation, the electrons (e^-) of BiOI were excited from the valence band to the conduction band, leaving holes (h^+) in the valence band. Then, the photo-induced electrons could transfer from the conduction band of BiOI to that of MnO_2. Thus, the photo-induced electrons were enriched on MnO_2 and the holes were reserved on BiOI, which effectively separated the photo-induced electrons and holes in space and prolonged the lifetime of the carriers. Both the holes and electrons were dominant active centers for visible-light catalysis.

4. Conclusion

In conclusion, we have reported a simple, highly efficient and economical way to synthesize a BiOI/MnO_2 composite. The optimum BiOI/MnO_2 composite (5/1) demonstrates a maximal photocatalytic degradation efficiency of 99.18% under simulated solar light irradiation for RhB aqueous solution (100 mL, 20 mg L^{-1}) within 60 min. The excellent photocatalytic performance is ascribed to the unique flower-like structure and synergistic effect between BiOI and MnO_2. Our results show that the BiOI/MnO_2 composite has broad application prospects in the field of photocatalytic degradation of organic pollutants due to its low cost and high catalytic performance.

Conflicts of interest

There are no conflicts to declare.

Acknowledgements

We express the great appreciation of the funding support by the National Scientific fund of Heilongjiang Province (No. GFQQ2440501215), Harbin Science and Technology Innovation Fund (No. 2015RQQXJ030).

Notes and references

1 M. Yan, Y. Hua, F. Zhu, W. Gu, J. Jiang, H. Shen and W. Shi, *Appl. Catal., B*, 2017, **202**, 518–527.
2 Y. Cong, Y. Ji, Y. Ge, H. Jin, Y. Zhang and Q. Wang, *Chem. Eng. J.*, 2017, **307**, 572–582.
3 Q. Han, R. Wang, B. Xing, T. Zhang, M. S. Khan, D. Wu and Q. Wei, *Biosens. Bioelectron.*, 2018, **99**, 493–499.
4 H. Wang, Y. Liang, L. Liu, J. Hu, P. Wu and W. Cui, *Appl. Catal., B*, 2017, **208**, 22–34.
5 L. Lin, M. Huang, L. Long, Z. Sun, W. Zheng and D. Chen, *Ceram. Int.*, 2014, **40**, 11493–11501.
6 J. M. Montoya-Zamora, A. Martínez-de la Cruz and E. López Cuéllar, *J. Taiwan Inst. Chem. Eng.*, 2017, **75**, 307–316.
7 J. Lu, J. Wu, W. Xu, H. Cheng, X. Qi, Q. Li, Y. Zhang, Y. Guan, Y. Ling and Z. Zhang, *Mater. Lett.*, 2018, **219**, 260–264.
8 P. Intaphong, A. Phuruangrat, S. Thongtem and T. Thongtem, *Mater. Lett.*, 2018, **213**, 88–91.
9 H. Huang, Y. He, X. Du, P. K. Chu and Y. Zhang, *ACS Sustainable Chem. Eng.*, 2015, **3**, 3262–3273.
10 X. Zhang, L. Z. Zhang, T. F. Xie and D. J. Wang, *J. Phys. Chem. C*, 2009, **113**, 7371–7378.
11 J. Cao, B. Xu, B. Luo, H. Lin and S. Chen, *Catal. Commun.*, 2011, **13**, 63–68.
12 Y. Yang, Z. Zeng, C. Zhang, D. Huang, G. Zeng, R. Xiao, C. Lai, C. Zhou, H. Guo, W. Xue, M. Cheng, W. Wang and J. Wang, *Chem. Eng. J.*, 2018, **349**, 808–821.
13 B. Y. Yin, S. Z. Zhang, Y. Jiao, Y. Liu, F. Y. Qu and X. Wu, *CrystEngComm*, 2014, **16**, 9999–10005.
14 B. Nanda, A. C. Pradhan and K. M. Parida, *Microporous Mesoporous Mater.*, 2016, **226**, 229–242.
15 W. Yu, T. Liu, S. Cao, C. Wang and C. Chen, *J. Solid State Chem.*, 2016, **239**, 131–138.
16 Y. Wang, H. Sun, H. M. Ang, M. O. Tadé and S. Wang, *Appl. Catal., B*, 2015, **164**, 159–167.
17 P. Xia, B. Zhu, B. Cheng, J. Yu and J. Xu, *ACS Sustainable Chem. Eng.*, 2017, **6**, 965–973.
18 S. Q. Liu, H. Z. Liu, G. H. jin and H. Yuan, *RSC Adv.*, 2015, **5**, 45646.
19 C. Guo, J. Xu, Y. He, Y. Zhang and Y. Wang, *Appl. Surf. Sci.*, 2011, **257**, 3798–3803.
20 S. Gao, C. Guo, J. Lv, Q. Wang, Y. Zhang, S. Hou, J. Gao and J. Xu, *Chem. Eng. J.*, 2017, **307**, 1055–1065.
21 J. Dong, G. Lu, F. Wu, C. Xu, X. Kang and Z. Cheng, *Appl. Surf. Sci.*, 2018, **427**, 986–993.
22 J. Jiang, H. Wang, X. Chen, S. Li, T. Xie, D. Wang and Y. Lin, *J. Colloid Interface Sci.*, 2017, **494**, 130–138.
23 J. Yan, Z. Fan, T. Wei, W. Qian, M. Zhang and F. Wei, *Carbon*, 2010, **48**, 3825–3833.
24 J. Hou, K. Jiang, M. Shen, R. Wei, X. Wu, F. Idrees and C. Cao, *Sci. Rep.*, 2017, **7**, 11665.
25 P. Liu, Y. Zhu, X. Gao, Y. Huang, Y. Wang, S. Qin and Y. Zhang, *Chem. Eng. J.*, 2018, **350**, 79–88.
26 Y. Zhang, S. Liu, Z. Xiu, Q. Lu, H. Sun and G. Liu, *J. Nanopart. Res.*, 2014, **16**, 2375.
27 T. B. Li, G. Chen, C. Zhou, Z. Y. Shen, R. C. Jin and J. X. Sun, *Dalton Trans.*, 2011, **40**, 6751–6758.
28 H. Yamashita, Y. Ichihashi, S. G. Zhang and Y. Matsumura, *Appl. Surf. Sci.*, 1997, **121/122**, 305–309.
29 Y. Yu, C. Cao, H. Liu, P. Li, F. Wei, Y. Jiang and W. Song, *J. Mater. Chem. A*, 2014, **2**, 1677–1681.
30 A. C. Gutierrez and T. F. Jamison, *Org. Lett.*, 2011, **13**, 6414–6417.
31 S. Bai, H. Chu, X. Xiang, R. Luo, J. He and A. Chen, *Chem. Eng. J.*, 2018, **350**, 148–156.